NTNU

Norwegian University of
Science and Technology

Design, Optimization and Analysis of a Single Rotor Magnetic Gear Electric Machine

Gunnar Charlie David Bjørk

Master of Energy and Environmental Engineering
Submission date: June 2017
Supervisor: Robert Nilssen, IEL

Norwegian University of Science and Technology
Department of Electric Power Engineering

Design, Optimization and Analysis of a Single Rotor Magnetic Gear Electric Machine

Charlie Bjørk
Faculty of Information Technology and Electrical Engineering,
Department of Electric Power Engineering,
NTNU - Norwegian University of Science and Technology,
Trondheim - NO

***Abstract*—Magnetic gears have recently become serious contenders for mechanical gears in low speed applications that require high torque. A magnetic gear features benefits such as inherent overload protection and low maintenance, while having torque handling capabilities similar to mechanical planetary gears. In this thesis an integrated magnetic gear brushless permanent magnet machine is designed, optimized and analyzed for use in marine applications. This type of machine uses the principles of a magnetic gear within a synchronous machine, and preliminary investigations have shown that they exhibit very good torque capabilities.**

The machine is developed through a careful design process, which is validated by the finite element method in COMSOL multiphysics. During the design process heavy calculations are performed on a supercomputer, which enables the computation of very large parametric sweeps. Parallel to manually designing a machine, a particle swarm optimization of the same design, under similar limitations is performed on a supercomputer. The results from both design processes are compared and it is concluded that the particle swarm method is a powerful tool that should be used actively during design. However it is also found that the particle swarm optimization should be controlled and iterated by a machine designer, in order to make the design feasible in practice.

The resulting machine designs achieve torque densities of 98.8 kNm/m^3 and 105.9 kNm/m^3 respectively, which make them relevant contenders to existing direct-drive solutions in terms of compactness. However low power factors of 0.187 and 0.188 means that they require large and expensive converters which is undesired in marine applications. Along with a quantitative analysis of losses in the machines the results are also reviewed qualitatively.

An alternative method of describing the principle of the magnetic gear is adopted from the Vernier reluctance machine, and the connection between these is clearly shown. This will hopefully make the operating principle more intuitive to understand.

NOMENCLATURE

PM	**Permanent magnet**
LSR	**Low speed rotor**
FEM	**Finite element method**
MG	**Magnetic Gear**
GE-MGEM	**General Electric MG Electric Machine**
PDD	**Pseudo Direct Drive**

I. INTRODUCTION

Magnetic gears have recently received a fair bit of scientific attention due to promising performance. They avoid many of the drawbacks of mechanical gears due to the input and output rotor not being mechanically connected. These include inherent overload protection, reduced friction, reduced transmission of shaft vibrations, reduced mechanical maintenance and reduced risk of contamination from lubrication oil. The inherent overload protection is especially interesting for use in marine propulsion, e.g. if a propeller hits ice the overload will translate into slip in the gear instead of depreciating the gears.

This thesis is inspired by the high performing magnetic gear proposed in [1] and depicted in Fig. 1. This paper has inspired many recent papers, and a study comparing magnetic gears to mechanical planetary gears [2] showed that they can match or even surpass the performance of their mechanical counterparts. An evolution of the magnetic gear has been to integrate it into

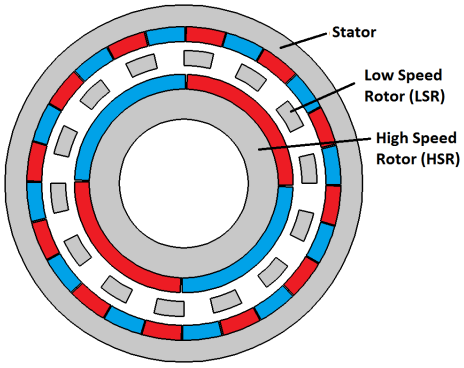

Fig. 1. Radial cross section of a pure magnetic gear

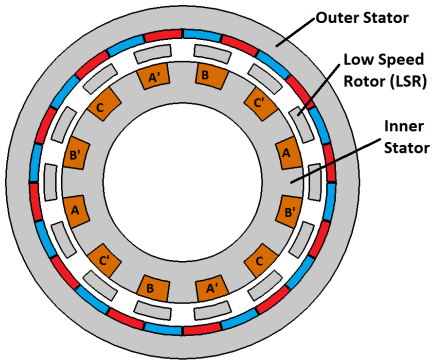

Fig. 2. Radial cross section of the GE magnetic gear electric machine

a synchronous permanent magnet (PM) machine and thereby removing the gearbox altogether. A General Electric (GE) patent [3] proposed to substitute the high speed rotor of a magnetic gear with three phase armature windings, as depicted in Fig. 2. Other papers proposed to integrate a magnetic gear in its entirety into a synchronous machine, keeping both rotors while having both two [4] and three [5] air-gaps. The version with two rotors and two air-gaps was dubbed the "pseudo direct drive" PDD and is depicted in Fig. 3.

A large PDD designed in [6] for marine propulsion achieved a torque density of >100 kNm/m^3 and a PF of ∼0.9. Compared to regular state of the art PM machines, which may have torque densities as high as 60 kNm/m^3, this is an extraordinary result. Transverse flux machines have achieved torque densities of up to 80 kNm/m^3 [6], but suffers from poor PFs which increases converter size and cost.

Due to the reported torque performance of the PDD it was selected for a comparison with the GE topology [3] in a previous comparative analysis performed by the author [7]. The GE topology, hereby referred to as the General Electric magnetic gear electric machine (GE-MGEM), performed considerably better than the PDD measured by its torque density. It also featured benefits such as less PMs and a simpler mechanical structure. This resulted in a desire to design, optimize the design and analyze the machine more throughout. Therefore the purpose of this thesis is to design such a machine intended for use in marine applications. Both an iterative classical design process and a full particle swarm optimization algorithm is performed on the model. A supercomputer is utilized for heavy computations. The resulting design proposals from both methods are then analyzed and benchmarked. Simulations are performed by the finite element method (FEM) in COMSOL multiphysics 5.2a.

Practically this thesis starts with a literature review of the magnetic gear and corresponding magnetic gear machines, put into a historical context. This is followed by a throughout explanation of the working principle, where this is explained in two different ways, and the connection to Vernier machines is examined. The FEM modeling specifics are described in a section, and the developed model is used for the design optimization and analysis of the proposed designs. Manual optimization is performed in a process that consist of making a hypothesis of how a parameter effects the torque performance and then evaluating this with FEM simulations. In a way the simulations act as an experiment made to validate or discard a hypothesis, in accordance with the hypothetico deductive scientific method [8].

II. Background

The specific design chosen in this thesis is directly based on the pure magnetic gear depicted in Fig. 1. This design has been available for quite some time, but has not been given a large amount of attention until recently. A short historical overview is therefore given before the reasoning behind choosing this specific topology is revealed. Additional magnetic gear machine topologies relevant to this paper are briefly reviewed.

A. Magnetic Gears

As explained in [7] the magnetic gear in its current form, depicted in Fig. 1, was described in a 1964 US patent [9]. However this design did not receive notable attention in scientific papers, perhaps due to poor performance of PMs at the time. Different papers [10] and [11] described magnetic gears in the 1980s, but they suffered from poor performance either from poor magnetic material or from restraints related to the magnetic circuit design.

Development of high coercivity rare earth PMs in the 1980s [12] made it possible to improve the performance of magnetic gears. In a design proposed in 2001 [1] the magnetic circuit design of [9] was combined with the high performing PMs and it achieved very promising performance. The radial cross section of this design is depicted in Fig. 1 and it forms the basis for the machine analyzed in this thesis. Several studies of this gear, among them [13] and [14], showed that the magnetic gear is a viable option for mechanical gears. A comparative study between mechanical planetary gears and the magnetic gear was conducted in [15]. It concluded that the torque density of a magnetic gear can match, or even surpass that of its mechanical counterpart. It was shown that safety factors greatly affect the sizing of mechanical gears. Magnetic gears however, have benefits compared to mechanical gears when it comes to fault situations and do not need such large safety factors.

B. Magnetically Geared Electric Machines

In 2006 General Electric filed a patent application describing a magnetic gear where the inner high speed rotor had been replaced by a second stator with armature windings, as depicted in Fig. 2. These windings produced a rotating field similar to that from the magnetic gear high speed rotor. A 2008 paper [16] described this particular design scientifically and it was further analyzed in [17]. In these papers it is concluded that the design possesses distinct advantages for direct-drive applications that require high torque at low speed. In this thesis references to this topology will be made by the abbreviation GE-MGEM.

In another topology introduced in [4] both rotors from a magnetic gear are integrated into an electric machine, as depicted in Fig. 3. This topology has two rotors, one HSR and one LSR similar to a pure magnetic gear, but with additional armature windings on the stator. In this thesis, references to this topology will be made by the abbreviation PDD for simplicity.

C. Additional Magnetic Gear Machine Topologies

Additional to the two topologies mentioned so far, there are other topologies that utilize the "magnetic gearing" effect. The common denominator for machines following this effect is that they have similar air-gap space harmonics, that follow from the same equations. These equations are described in section

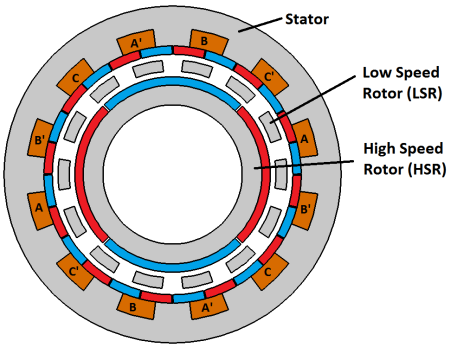

Fig. 3. Radial cross section of a magnetic gear "Pseudo Direct Drive" machine

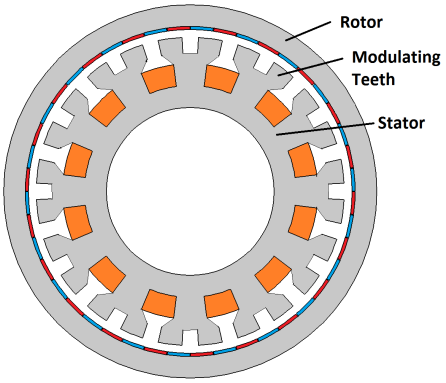

Fig. 4. Radial cross section of a Vernier PM machine

III and describe the relationship between the number of armature pole-pairs, PM pole-pairs and modulating pole-pieces. A throughout study of magnetic gear machine topologies is presented in [18] and in this paper, only those most relevant to the GE-MGEM are considered.

Vernier PM machines where noted in [19] to achieve high torque due to a "magnetic gearing" effect. A Vernier PM machine is depicted in Fig. 4, and here the stator teeth have a similar function as the pole-pieces of a magnetic gear. The relation between the number of armature poles, stator teeth and rotor PMs follows the same relation as for the GE-MGEM. The main difference from the GE-MGEM is that the Pole-Pieces are attached to the stator in the Vernier machine, while the outer stator is used as a rotor, thus removing one air-gap. Early non PM Vernier reluctance machines [20] achieved very low power factors, in the order 0.15 to 0.20 [21], but in more recent papers, power factors of $\sim$0.7 [22] has been claimed.

Another topology that uses the magnetic gear effect was introduced in [18] and dubbed the "Partitioned Stator Switched Flux machine". An analysis of this machine was performed in [23] and the topology from that study is depicted in Fig. 5. A Torque density of 97 kNm/m^2 was achieved, which is similar to that achieved for the GE-MGEM. The space harmonics in the air-gap of this machine is similar to that of the GE-MGEM even though the inner stator PMs are internal and displaced 90 °, and it also follows the same governing equations.

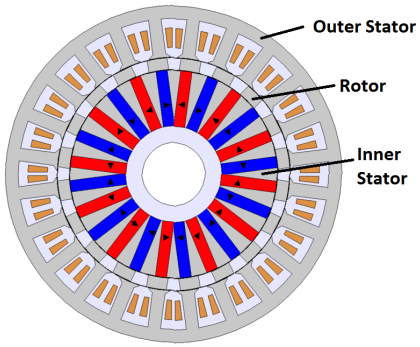

Fig. 5. Radial cross section of a Partitioned Stator Switched Flux machine. Figure from [23]

III. Mechanical structure and operational principle

The GE-MGEM operates after the same principles as the pure magnetic gear described in [1] and [14]. However this machine only has one rotor as depicted in Fig. 2, compared to two rotors for the magnetic gear depicted in Fig. 1. The high speed rotor of the magnetic gear is replaced by armature three phase windings, which produce a rotating magnetic field with the same rotational velocity as the high speed rotor.

Essential to the operation of the GE-MGEM is the modulation of the armature field across the ferromagnetic pole pieces (PP). These pole pieces act as a filter that adds or remove certain harmonic space components depending on the direction of power transfer. Starting from the armature magneto motive force, which is set up by a sinusoidal current, the largest space harmonic component adjacent to the inner-stator has the same number of pole-pairs as the fundamental component of the armature field. However, after crossing the pole-pieces the largest harmonic component adjacent to the outer stator occurs at a higher pole-pair number. This high pole-pair space harmonic interacts synchronously with the stator PMs and creates synchronous torque between the iron pole-pieces and the PMs.

Two different approaches will be taken to explaining the working priniciple of the GE-MGEM. First a more intuitive explanation based on the reluctance principle will be used. Thereafter a method of mathematically describing the modulating effect of the pole-pieces is presented. Before all this, the mechanical structure of the machine is described.

A. mechanical structure

Structurally the GE-MGEM has one inner stator, containing the armature windings, and one outer stator with a set of PMs. Between these a rotor consisting of a number of ferromagnetic pole-pieces is situated. Fig. 2 shows the radial cross section of such a machine, where these parts are depicted. An axial cross section of the machine is depicted in Fig. 6. It is shown in this figure that three bearings are sufficient for operating this machine depending on the material strength of the connection at the right hand side. Cooling channels can be drilled out

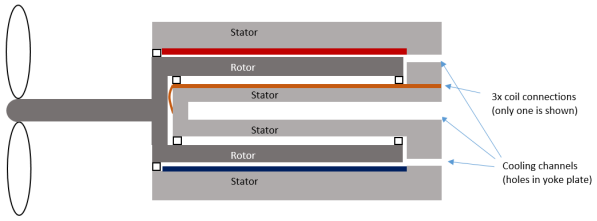

Fig. 6. Axial cross section of the GE-MGEM

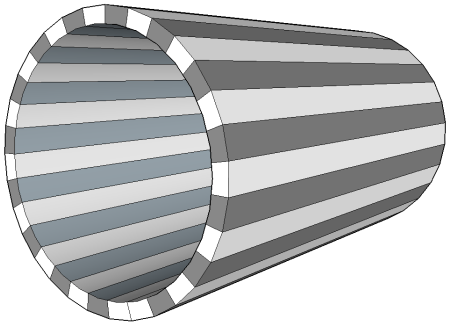

Fig. 7. 3D drawing of the rotor

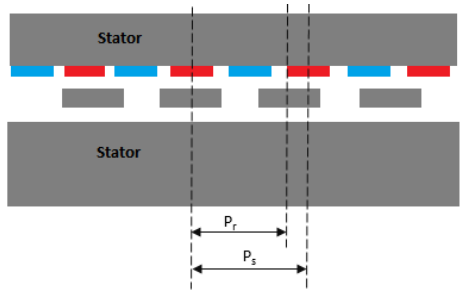

(a) Rotor position 1

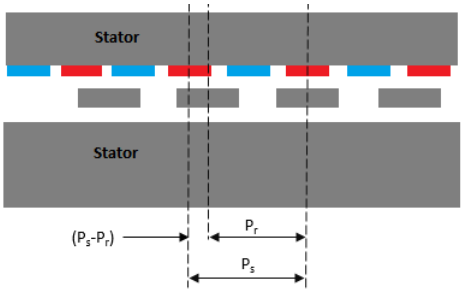

(b) Rotor position 2

Fig. 8. A sequence of the rotor rotating an angle $(p_s - p_r)$, where p_s and p_r represent the stator slot-pitch and rotor pole-pitch respectively

in the plate to provide air-flow through the air-gaps of the machine.

Structural integrity of the rotor is achieved by using non magnetic material with relative permeability ~ 1 between the pole-pieces. A three dimensional drawing of such a rotor is provided in Fig. 7. Due to the strength requirements, it may be necessary to use non-laminated ferromagnetic material, which will contribute to increased losses.

B. Principle explained after the reluctance principle

As mentioned in section II the GE-MGEM has similarities with the Vernier PM machine, and this similarity was pointed out in [24]. The Vernier PM machine is a further evolution of the Vernier Reluctance machine [25], which is more thoroughly described in [20] and [21]. An explanation of the working principle of the GE-MGEM will be presented, inspired by the explanation given for the vernier reluctance machine.

Fig. 8 shows a small linearized section of the GE-MGEM. Stator slot-pitch and rotor pole-pitch are denoted p_s and p_r respectively. The figure shows the rotor before and after it has been rotated a distance $(p_s - p_r)$.

Essential to this explanation is the axis of maximum permeance, which is the path of least reluctance in the magnetic circuit. The red and blue PMs has alternating remanent flux density in the radial direction. Thus the easiest way for a flux line to cross the air-gaps from the inner stator is through the pole-piece aligned with it and through the PM pointing in the same direction. This corresponds to the left dashed line in Fig. 8a. After rotating the rotor a distance $(p_s - p_r)$ to the right the preffered flux path follows the rightmost dashed line referring to Fig. 8b.

In this way the rotation of the axis of least reluctance and the magneto motice force (mmf) rotate synchronously, while the rotor rotates at a fraction of the mmf speed. The rotor pole-pieces wish to constantly align with the axis of least reluctance while the mmf keeps rotating, and this creates torque in the machine. This phenomenon is also known as reluctance torque.

The ratio of the rotational speed of the axis of least permeance to the rotational axis of the rotor becomes the gear ratio

$$GR = \frac{p_s}{p_s - p_r}, \tag{1}$$

where p_s is the stator slot-pitch and p_r is the rotor pole-pitch, i.e. the circumferential distance between the center of two adjacent pole-pieces. The pitch is given by the number of PM pole-pairs, P_o, on the outer stator and the number of rotor pole-pieces, N_s, along a full circumference of the machine, Y. Substituting $p_s = Y/P_o$ and $p_r = Y/N_s$ into (1) gives

$$GR = \frac{N_s}{N_s - P_o}. \tag{2}$$

In a machine consisting of a number of PM pole-pairs and ferromagnetic pole-pieces there will be a certain periodicity to the axis of least reluctance. Starting from a pole-piece that is in alignment with a PM with the correct remanence, i.e. the leftmost line in Fig. 8a, the displacement of the rotor pole-pieces from alignement with corresponding PMs for the following pole-pieces becomes

$$(p_s - p_r), 2 \cdot (p_s - p_r), ..., n \cdot (p_s - p_r). \tag{3}$$

Alignment reoccurs when the displacement is equal to one rotor pole-piece-pitch, i.e. when $n \cdot (p_s - p_r) = p_s$. Solving for n and substituting for p_s and p_r similarly to before yields

$$n = \frac{p_s}{p_s - p_r} = \frac{N_s}{N_s - P_o}. \tag{4}$$

This represents the number of rotor pole-pieces between each repeating axis of least reluctance. It is also the number of pole-pieces that has to be covered by the mmf wave from a full electrical period of the armature current. Thus the pole-pair number of the armature windings, P_i, can be calculated as

$$P_i = \frac{N_s}{N_s/(N_s - P_o)} = N_s - P_o. \tag{5}$$

Substituting this into (2) gives the gear ratio of the machine

$$GR = \frac{N_s}{P_i}. \tag{6}$$

It is actually slightly incorrect to call the path which the flux would follow for the path of least reluctance because the reluctance of PMs is equal, independent of the direction of their remanence. In the above explanation the PMs with opposite remanence than the field crossing the air-gaps have simply been ignored. This is plausible in practice because the PM with remanent flux density in the same direction as the armature flux will be the "easiest" path for the flux to follow.

C. Principle explained with modulating equation

Another quantitative explanation of the working principle is presented in [14]. This explanation defines a modulating function that describes the modulating effect the ferromagnetic pole-pieces have on both the magnetic field from the armature and the PMs. The field experienced at a distant r from either field source is a product of two sinuses, where the first term represents the field without pole-pieces and the second term represents the modulating function of the pole-pieces. For the radial component this is

$$\begin{aligned} B_r(r,\theta) = & \\ & \Big(\sum_{m=1,3,5,\ldots} b_{rm}(r)cos(mp(\theta - \Omega_r t) + mp\theta_0)\Big) \\ & \times \Big(\lambda_{r0} + \sum_{j=1,2,3,\ldots} \lambda_{rj}(r)cos(jn_s(\theta - \Omega_s t))\Big). \end{aligned} \tag{7}$$

Similarly the circumferential component is

$$\begin{aligned} B_\theta(r,\theta) = & \\ & \Big(\sum_{m=1,3,5,\ldots} b_{\theta m}(r)sin(mp(\theta - \Omega_r t) + mp\theta_0)\Big)\times \\ & \Big(\lambda_{\theta 0} + \sum_{j=1,2,3,\ldots} \lambda_{\theta j}(r)cos(jn_s(\theta - \Omega_s t))\Big). \end{aligned} \tag{8}$$

Here p is the number of corresponding pole-pairs and n_s is the number of pole-pieces. Ω_r and Ω_s are the rotational velocities of the relevant magnetic field and the pole-pieces respectively. The Fourier coefficients of the flux density distribution in radial and circumferential direction are b_{rm} and $b_{\theta m}$ and the modulating Fourier coefficients of the flux densities are λ_{rj} and $\lambda_{\theta j}$.

Rewriting (7) and (8) can be done to produce (9) [14]. This equation gives the number of space harmonic pole-pairs adjacent to one of the field sources due to the modulation of the field from the other source, i.e. the field from either the inner stator armature current or from the outer stator PMs. For the GE-MGEM this would for example be the resulting space harmonics adjacent to the outer PMs due to the modulation of the armature field.

$$\begin{aligned} p_{m,k} &= |mp + kn|. \\ m &= 0, 1, 2, ..., \infty \\ k &= 0, \pm 1, \pm 2, ..., \pm\infty \end{aligned} \tag{9}$$

Here $p_{m,k}$ is the number of resulting space harmonic pole-pairs associated with the m and k harmonic, p is the number of pole-pairs and n is the number of pole pieces. The largest harmonics occur for m=1 and k=-1 and thus the equation guarding the number of PM pole-pairs and the number of pole-pieces is given by

$$P_o = |P_i - N_s|, \tag{10}$$

where P_o is the number of outer PM pairs, P_i is the number HSR PM pairs and N_s is the number of pole-pieces. During design it is important to match the number of outer PM pairs with the number of space-harmonic pole-pairs resulting from the modulation of the armature field. By adding the assumption that N_s is always larger than P_i and rearranging (10) it leads to

$$P_i = N_s - P_o, \tag{11}$$

which is similar to what was found in (5). Rotational speed of the space harmonic field can be deduced in a similar manner as shown in equation (12).

$$\Omega_{m,k} = \frac{mP_i}{mP_i + kN_s}\Omega_r + \frac{kN_s}{mP_i + kN_s}\Omega_s. \tag{12}$$

Here Ω_r and Ω_s are the rotational velocities of the PM field and the pole-pieces respectively. Setting m=1 and k=-1, while letting $\Omega_s = 0$ gives a gear ratio of

$$G_r = \frac{N_s - P_i}{P_i}, \tag{13}$$

Where N_s is the number of pole pieces, P_i is the number of inner pole pairs and P_o is the number of PM pole pairs, which in this case is on the output rotor. Magnetic flux crossing an air-gap between two ferromagnetic iron pieces creates a pulling force acting on both components in opposite direction [26]. This means that there is an equal force pulling on the PM stator and on the ferromagnetic pole-pieces, but in opposite directions, implying that both the PMs and the ferromagnetic pole pieces can be used as the output rotor given that the other is held stationary. However, as pointed out in [14] this results in different gear ratios depending on which is chosen as the

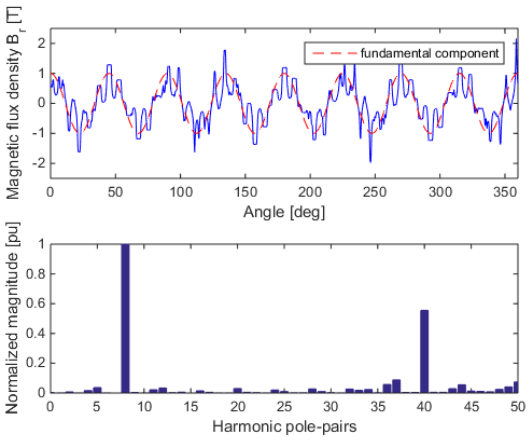

Fig. 9. Flux density adjacent to the inner stator as a function of angular position, along with corresponding harmonic spectrum

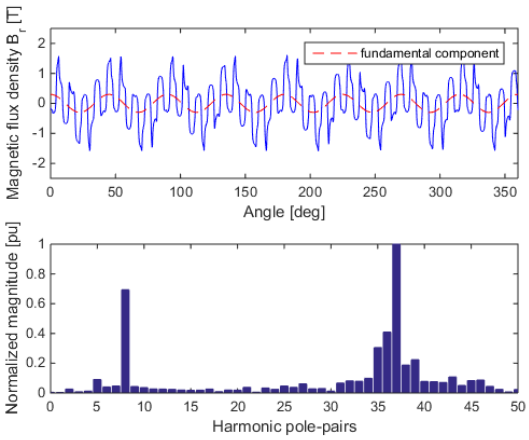

Fig. 10. Flux density adjacent to the outer stator as a function of angular position, along with corresponding harmonic spectrum

output rotor. With stationary PMs and rotating pole-pieces, the gear ratio is as given in (14)

$$G_r = \frac{n_s}{p_i}. \tag{14}$$

In this thesis the pole-pieces will be chosen as the rotor as this gives a higher gear-ratio, and hopefully a better torque density.

It is clear that the equation for Gear-ratio (14) and the relation between pole numbers (11) are equal to the equations developed in section III-B, namely (6) and (5).

D. FEM verification of working principle

A stationary simulation was run for the GE-MGEM geometry in COMSOL multiphysics to generate the flux density distribution in both air-gaps. A fast fourier transform (fft) was performed on this distribution, for a topology with $P_i = 8$, $N_s = 45$ and $P_i = 37$.

Fig. 9 shows the flux density distribution adjacent to the inner stator. It is expected that the fundamental 8 pole-pair component from the armature field is the largest harmonic component, and this is confirmed by the harmonic spectrum shown in the bottom of the figure. Interestingly a large component is present with a pole-pair number of 40. This component was unexpected, and it is not believed to contribute to torque creation. Instead it may cause problems such as losses and vibrations.

The flux density distribution adjacent to the PMs on the outer stator is depicted in Fig. 10, along with its harmonic spectrum. This clearly shows the effect of the modulating pieces with the largest space harmonic component appearing at 37 pole-pairs, as expected from (10). Coinciding with this is a reduction of the fundamental component of the armature field, such that the high pole-pair harmonic becomes the dominating flux component in the machine. It is this component that causes the torque production of the machine by interacting synchronously with the PM pole-pairs. These plots also indicate that most of the torque production is taking place in the outer air-gap.

IV. FEM MODELLING

COMSOL Multiphysics 5.2 is used for all the simulations in this thesis. For analyzing big data sets Matlab R2014b is used. A description of the specific FEM modeling will follow, which will make it easier to reproduce the simulations for verification.

COMSOL Multiphysics is a general purpose physics simulator based on advanced numerical methods. It makes it possible to solve advanced nonlinear unbalanced partial differential equations that are impossible to solve analytically and which would be largely inconvenient to solve numerically by hand. E.g. Navier-Stokes equation in fluid dynamics or Amperes law in electromagnetics.

Comsol is structured in a tree form with global definitions affecting the Component nodes. The study node controls how the components should be analyzed. Finally the results node enables post prosessing of the simulated data, such as plotting and data export.

The model in this thesis is a 2 dimensional radial cross section of the GE-MGEM as depicted in Fig. 2 and described in section III. In Comsol this geometry is quite straightforward to produce. Every variable is parameterized in global definitions and the geometry adapts automatically to changes in these. Every domain has to be assigned a material.

Due to the nature of pole-number selection, guarded by (10), symmetry is only available for a select few combinations. The model therefore includes the entire circumference of the machine. Due to this the model becomes quite large and taxing on computational power, especially when performing time simulations. Therefore the design optimizations are performed with stationary simulations before the resulting designs are analyzed in the time domain.

A. Materials used

The materials used are found in COMSOLs built in library, with the exception of the permanent magnets which are

defined manually. Permanent magnets are defined with relative permeability $\mu_r = 1.05$, conductivity $\sigma = 0.667 \cdot 10^6$ and relative permittivity $\epsilon_r = 1$, based on material properties of NdFeB. The steel used is non grain oriented, Silicon Steel 50PN270.Normal copper is used as the winding material, while regular air is used for the air-gap.

Laminated steel can be used for the back-iron (yoke) of both stators, but the rotor pole-pieces may have to be non-laminated for the sake of material strength. Maximum flux density is limited by the effects of saturation, and the B-H curve that determines this is depicted in appendix B-B.

B. Torque calculation

Torque is normally calculated in one of two different ways, which yield approximately the same results. The built in force calculation uses Maxwell stress tensors to calculate torque around the boundary of the iron pole-pieces.

Using Maxwell stress tensors, torque is calculated as a surface integral surrounding the rotor like a cylinder in the air-gap. For a two dimensional model, this translates to a line integral in the air-gap. Under ideal circumstances the torque should be the constant, independent of the line integral radius, as long as the line is in the air-gap. However as pointed out by Arkkio [27] this is not the case in practice and variations of torque for the integration at different radiuses in the air-gap can be noticeable. The Maxwell stress tensor line integral can be expressed as

$$T_e = \frac{1}{\mu_0} \int_0^{2\pi} r^2 B_r B_\phi d\phi, \tag{15}$$

where T_e is torque, B_r is the radial flux density and B_ϕ is circumferential flux density. r is the radius for which the function is being evaluated and μ_0 is the universal constant for permeability in vacuum.

Arkkio pointed out another method developed in [28] that replaces the line integral with a volume integral over a hollow shell surrounding the rotor. In a two dimensional case this becomes a surface integral of a disk situated in the air-gap. The torque equation thus becomes

$$T_e = \frac{L}{\mu_0 (r_s - r_r)} \int_{S_{ag}} r B_r B_\phi dS, \tag{16}$$

where T_e is torque, L is machine length, r_s is outer shell radius, r_r is inner shell radius B_r is radial flux density and B_ϕ is circumferential flux density. r is the radius for which the function is being evaluated. This method has been proven by Arkkio, and others, to give more reliable results and to be less prone to numerical noise than the maxwell stress tensors. However in the case of the GE-MGEM model this method required additional two domains in each air-gap, which increased the mesh creating time. This proved to be critical for the time consumption during the design optimization simulations, which required the model to rebuild the mesh multiple times for different model parameters. Therefore the built in method based on eq. (15) is used in this paper.

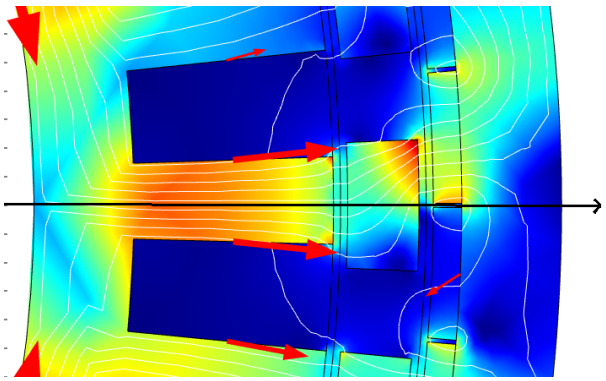

Fig. 11. Optimal start angle air-gap flux

C. Optimal Pole Piece start angle

The simulation is carried out at synchronous speed at synchronous frequency. For synchronous machines induced torque can be expressed as

$$\tau_{ind} = k B_R B_{net} \delta, \tag{17}$$

where k is a constant, B_R is the rotor flux density and B_{net} is the vector sum of the rotor and stator flux density [29]. δ is known as the torque angle and it is the same angle as the phase shift between the terminal voltage $\mathbf{V}_\phi$ and the internal generated voltage $\mathbf{E}_A$. This equation is not exact when accounting for magnetic saturation, however it is valid for qualitatively understanding machine operation.

From the equation it is clear that a certain rotor position will create the highest output torque and this position is essential to know for the parametric optimization of the machine. If this angle is wrong different designs will compete under different assumptions and it will be impossible to compare the results. Because of the nature of the GE-MGEM working principle it is quite complicated to describe this angle with the general machine concepts. Instead a qualitative explanation based on FEM simulations will be performed.

Simulations revealed that the optimal rotor start angle was achieved when a rotor pole-piece was aligned with the tooth of highest flux density, while this axis passed right in between an outer stator PM pole-pair. Referring to Fig. 11 the inner stator armature current is at its maximum in the A phase coil, which makes the resultant mmf vector point in a horizontal direction. Making a rotor tooth align with this flux vector assures that a maximum amount of flux is crossing the air-gap. However this does not in itself create torque, and it has to be combined with the correct position of the PMs on the outer stator. A sweep that rotated the PMs a full pole-pitch revealed that the highest torque was achieved when the axis of alignment passed right through the middle of an outer stator PM pole-pair. In Fig. 11 this axis is depicted as a black arrow. Fig 24 in appendix A shows the results of rotating the PM magnets while keeping the rest stationary.

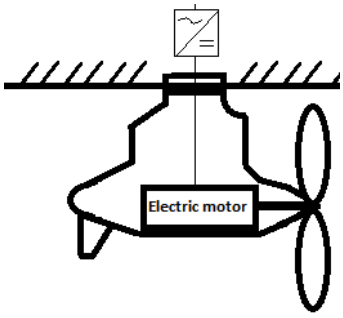

Fig. 12. Cross section of an outboard POD

TABLE I
APPLICATION REQUIREMENTS

Parameter	Requirement	Unit
Gear ratio	5-8	
Torque	200	kNm
Speed output	200	rpm
Power	4.2	MW
Max diameter	1.2	m

V. Application and Requirements

A. Applications

The GE-MGEM is designed for marine applications that require high torque at relatively low speed. A relevant application in this regard is for use in outboard PODs. A POD is depicted in Fig. 12 and consists of an electric motor driving a propeller for marine propulsion. PODs are also called azimuth thrusters if they in addition to provide propulsion provide steering by rotating the pods in horizontal direction. Outboard pods provide benefits compared to traditional propeller shafts by reducing shaft vibrations felt in the hull and freeing space aboard the vessel. Azimuth pods can also assist dynamic anchoring and docking by providing thrust in different directions. However, because the pods are submerged in water, the diameter of the pods is crucial for hydrodynamic reasons. It is therefore desireable with a machine that has a high torque density in order to minimize effect of underwater drag. A low power factor is also undesirable, because it increases the VA-rating and thus the volume occupied by the converter inside the ships hull.

B. Requirements

Based on the discussion in the last paragraph a list of requirements for the machine is given in table I. Values in this table represent boundaries for the design optimization.

VI. Design Optimization

A throughout design optimization process has been carried out for the GE-MGEM. First an optimal combination of pole-pair and pole-piece numbers was found before each parameter was evaluated through simulations. In addition to a manual design optimization a Particle Swarm Optimization (PSO) algorithm was performed for the model, and this is presented in section VII. The results from this was compared to the

TABLE II
OPTIMIZATION VARIABLES AND CONSTRAINTS FOR THESE

Parameter	initial value	$\mathbf{x} \in$
Inner pole-pairs P_i	6	[2, 30]
Outer pole-pairs P_o	29	$N_s - P_i$
Rotor pole-pieces N_s	35	[12, 150]
Yoke thickness inner stator	0.03	[0.01, 0.1]
Slot thickness	0.07	[0.01, 0.1]
Slot ratio	0.5	[0.1, 0.9]
Inner air-gap length	0.005	[0.003, 0.020]
Rotor pole-piece thickness	0.025	[0.01, 0.1]
Pole-piece ratio	0.5	[0.1, 0.9]
Outer air-gap length	0.005	[0.003, 0.020]
PM thickness	0.01	[0.005, 0.025]
Stat PM ratio	0.97	[0.3, 1]
Yoke thickness outer stator	0.03	[0.01, 0.1]

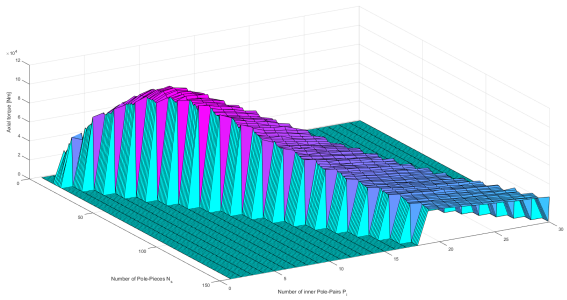

Fig. 13. Torque vs pole-pieces and pole-pairs

results from the manual design process before they where analyzed in the time domain.

The optimization objective is to find a set of parameters that maximize machine torque, based on the developed model. An objective function for the GE-MGEM can be written as

$$\underset{\mathbf{x}}{\text{maximize}} \quad \tau orque(\mathbf{x}),$$

where $\mathbf{x}$ are the parameters that are going to be optimized, constrained by the limits in table II. This objective function is used for both the manually performed design considerations and the Particle Swarm Optimization.

A. Pole-number selection

The number of pole-pairs on the stator and the number of pole-pieces on the rotor follows the relation in (10). Therefore one of the parameters is always given by two of the other.

In order to find a pole-number combination to base the design optimization on, a large parametric sweep was performed by utilizing the NTNU supercomputer Vilje [30]. The parameters that are changed are number of rotor pole-pieces N_s and armature pole-pairs P_i, which in turn determine the number of outer stator PM pole-pairs. A simulation was run that covers every combination of these parameters that satisfy the required gear-ratio requirements given in table I, and following the relation in (6). A Matlab script generating the list is given in appendix C.

Fig. 13 shows the results from this sweep. From the figure it is obvious that there is a clear maxima of this function. The

maximum torque is 111.82 kNm and occurs for $P_i = 8$ and $N_s = 45$ which gives a gear-ratio of 5.63.

Cogging torque in a PM machine is caused by the tendency of the rotor to prefer the position where the net force between the PMs and the iron is at its lowest. This is greatly affected by the number of pole-pairs and it is desirable to have a design where the forces acting on the iron pole-pieces by the PMs are balanced out. Cogging torque appears as ripple on the output torque of the machine, and is unfortunate for several reasons. The effect causes uneven torque output which again leads to vibrations that are undesired in most applications. High frequency vibrations also cause mechanical noise.

A cogging torque factor (CTF) was adapted from [31] to the magnetic gear in [14] and it can be adopted directly by the GE-MGEM. The CTF is not exact, but it gives an indication of how much cogging torque there will be for different pole-pair combinations. Adapted to the GE-MGEM the CTF can be written

$$f_{ct} = \frac{2P_i N_s}{N_{lcm}}, \tag{18}$$

where P_i is the number of armature pole-pairs and N_s is the number of rotor Pole-Pieces. N_{lcm} is the least common multiple between the two. Inserting the parameters for maximum torque results in $CTF = 2$ which is the lowest CTF obtainable with $P_i = 8$, and the gear ratio within the required limits $GR = 5.63$. The effect of cogging is seen as the torque ripples in the time domain simulation in section IX.

Electrical frequency of the armature depends on the gear ratio and pole-number selection. It was shown in [7] that it follows the relation

$$f_e = \frac{P_i GR n_{out}}{60} = \frac{N_s n_{out}}{60}, \tag{19}$$

where n_{out} is the constant rotational velocity of the rotor in rounds per minute (rpm). According to this relation the machine requires an electrical frequency of 150 Hz to drive the rotor at the required 200 rpm with the selected pole numbers.

B. Stator yokes thickness

While determining the pole-piece numbers, a simulation was run for a similar sweep, but without the effect of magnetic saturation in the iron. This achieved considerably better performance than the saturated counterpart which indicates that some parts of the machine is heavily saturated. The non saturated sweep is depicted in appendix A. Therefore a hypothesis that machine performance will increase by increasing the thickness of the back iron is tested in FEM.

Fig. 14 shows the results from increasing the thickness of the yoke of both stators simultaneously. It shows that the torque increases until the back-iron saturation no longer bottlenecks the machine. However it also shows that increasing the thickness above 3.5 cm actually decreases the torque performance of the machine. Studying the flux lines for the case with thicker yokes reveals that less flux crosses the air-gap. It is instead looping around in the inner stator. The reason for this could be that the saturation of the armature stator

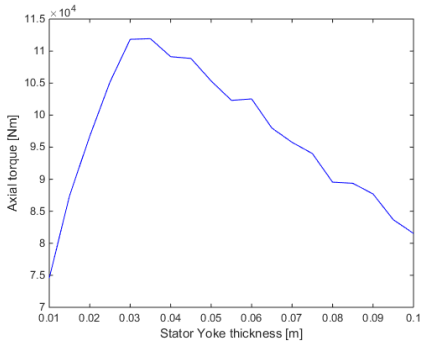

Fig. 14. Torque vs Yoke thickness of both stators

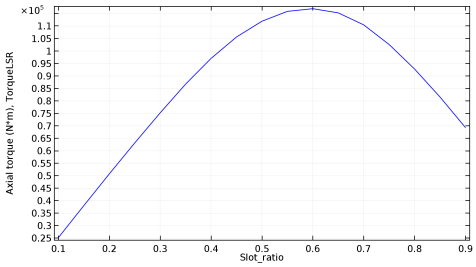

Fig. 15. Torque vs Slot-Ratio

yoke forces some of the flux to take longer paths through the iron, that naturally has a higher reluctance. This increases the required mmf for the flux to cross the air-gap and this flux therefore does not contribute to torque creation. As the machine has the same current input, this may instead increase the reactance of the machine, thus giving it a poorer power-factor. A yoke thickness of 3.5 cm is therefore chosen for both stators.

C. Slot-ratio

Slot-ratio is the ratio between tooth width and slot-pitch on the armature stator. A Slot-ratio of 0.5 indicates that the teeth are of the same width as the slots. Higher slot-ratios mean that the slots are wider than the teeth and vice versa. From the simulations of stator yoke thickness a hypothesis is formed claiming that tooth saturation is bottlenecking machine performance and that the performance will increase for a Slot-ratio lower than the initial 0.5. This is the case even though it means a reduction of the mmf, $F = NI$ [26].

The results from this sweep is depicted in Fig. 15. It indicates that a slot-ratio of 0.6 gives the highest torque, which contradict the initial hypothesis by not increasing for a lower Slot-Ratio. It seems like the teeth where not completely saturated and could endure a higher flux density. However a higher slot-ratio than 0.6 led to a decrease in torque due to saturation constraints. Studying the flux density of the machine for the different slot-ratios reveals that a slot-ratio of 0.6 has a flux density in the tooth that corresponds to heavy saturation according to the H-B curve of the material. A compromise slot-ratio of 0.55 is therefore chosen for this design.

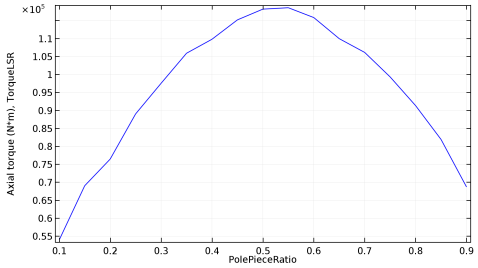

Fig. 16. Torque vs Pole-Piece Ratio

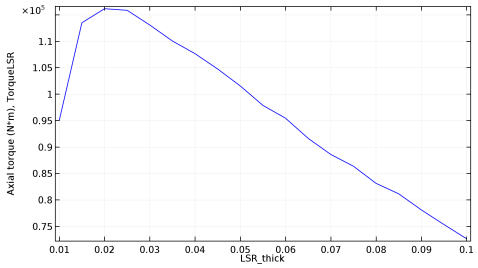

Fig. 17. Torque vs Pole-Piece thickness

D. Pole-Piece ratio

Pole-Piece ratio is the ratio of ferromagnetic pole-pieces to the pole-piece pitch on the rotor. E.g. a Pole-Piece ratio of 0.5 means that there is as much iron as there is low permeability material along the circumference of the rotor.

From the results depicted in Fig. 16 a pole-piece ratio of 0.5 gives the highest output torque and is therefore chosen.

E. Pole-Piece thickness

As mentioned in section III the rotor consists of a number of ferromagnetic pole-pieces, encapsulated in a low permeability material. It is nesessary for this mix to be able to withstand the high axial torque from the eletric machine along with any forces from the mechanical load. The thickness of the pole-pieces is therefore critical for the mechanical strength of the machine, and a more throughout mechanical analysis should be performed in order to determine weather the chosen thickness is feasible. In this thesis however, only electromagnetic part of the design is considered and these calculations are not performed. From an electromagnetic point of view a hypothesis is that thicker pole-pieces will result in a lower torque because it will be harder for the flux to cross from the inner to the outer stator.

Fig. 17 confirms the hypothesis that thinner pole-pieces results in higher torque. However for pole-pieces thinner than 2 cm this effect is reversed. A reason for this could be that the magnetic gearing effect depends on the modulation of the magnetic field over the pole-pieces, and if they become to thin this effect is dampened. Studying the calculated flux density adjacent to the outer PMs confirms this suspicion. Referring to Fig. 18 it is clear that the fundamental component from the armature field is larger for the thin pole-pieces than it is with thicker pole-pieces, thus confirming the effect on the

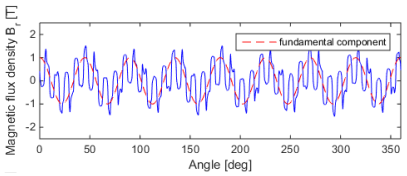

(a) Pole-piece thickness 1 cm

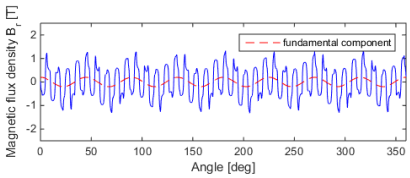

(b) Pole-piece thickness 10 cm

Fig. 18. Space flux density in the air-gap adjacent to the outer stator with varying pole-piece thickness

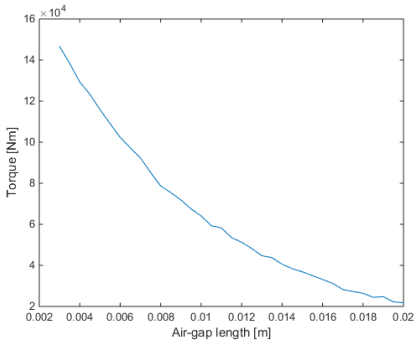

Fig. 19. Torque vs air-gap length

modulation. However, for the thick pole-pieces, output torque is lower according to Fig. 17 because less flux makes it across the air-gaps.

Based on the above discussion a pole-piece thickness of 2,5 cm is chosen. It is only slightly less than the maximum at 2 cm, and it will provide more mechanical strength.

F. Air-gap length

Air-gap length is the most critical parameter for air-gap flux density because of the high reluctance relative to iron [26]. It is therefore expected that output torque will increase for smaller air-gaps and decrease for larger. The air-gap length is therefore limited by mechanical considerations because it would be ideal to have almost no air-gap. In this thesis initial air-gap length is 5 mm, with the lower limit being defined at 3 mm. It is perhaps possible to have even smaller air-gaps, but it is comforting to have a certain knowledge of that the topology is realistically achievable. The machine is a double air-gap machine and the simulations are run with both air-gaps having the same length.

Torque vs air-gap length is depicted in Fig. 19. As expected the torque decreases as the air-gap length increases. An air-gap length of 5 mm is selected for analysis even though the best solution is 3 mm. The reason behind this is to analyze

the machine on a realistic foundation and 5 mm is reasonably simple to manufacture. However the result in Fig. 19 indicates that it is possible to achieve better performance by reducing the air-gap to 3 mm, and a more throughout mechanical analysis should be performed for this design. For power factor improvement, it may be necessary to decrease the load, in which case a smaller air-gap could be considered in order to still achieve a high torque density.

G. Final Proposed Parameters

Accumulated from all these considerations and simulations, are the selected variables for a final proposed design. These parameters are rendered in table III along with the results from the PSO algorithm. The design will be further analyzed in section IX.

TABLE III
FINAL PROPOSED DESIGN FROM BOTH MANUAL DESIGN AND FROM THE PSO ALGORITHM

Parameter	Manual design	PSO design
Inner pole-pairs P_i	8	4
Outer pole-pairs P_o	37	27
Rotor pole-pieces N_s	45	31
Yoke thickness inner stator	0.035	0.06
Slot thickness	0.07	0.0802
Slot ratio	0.5	0.5138
Inner air-gap length	0.005	0.0044
Pole-piece thickness	0.025	0.0419
Pole-piece ratio	0.5	0.4171
Outer air-gap length	0.005	0.0055
PM thickness	0.01	0.0236
Stat PM ratio	0.97	0.6510
Yoke thickness outer stator	0.035	0.0588
Gear-ratio	5.63	7.75

VII. PARTICLE SWARM OPTIMIZATION

As mentioned in the introduction a particle swarm optimization (PSO) algorithm was performed during the design of this machine as an alternative to an iterative design process. The algorithm is given upper and lower boundaries of each parameter and can freely choose solutions within these boundaries. Iterative approaches may return good results, but it can also miss out on some good solutions because of how different parameters affect each other dynamically. For example during the pole number selection in section VI-A, the yoke thickness was held at a constant initial value. This may have overlooked some better solutions that required a slightly thicker yoke due to saturation. The PSO however can change each parameter freely and might pick up this better solution. Accounting for this codependency is perhaps the greatest advantage of a pso over the iterative method.

The PSO optimization was done in collaboration with a fellow thesis student [32] who works with enabling technologies. Previous work on optimization of a magnetic gear [33] was limited by computational power, and therefore a supercomputer was used for the calculations.

This section will contain a short qualitative description of the PSO principle followed by a description of a PSO proposed design.

A. PSO Principle

PSO algorithms have become popular in electrical machine design [34] since being proposed in [35].

It originates from a desire to understand the mechanisms or underlying rules behind the fluid and synchronous movements of a flock of birds or similarly for other animals social behavior like fish schools or herds. The synchrony of flocking behavior is thought of as animals efforts to maintain optimum distance between themselves and their neighbors.

Following the natural example the PSO algorithm starts by initializing each agent in a population within a solution space, assigning each of them a position and a directional velocity. The agents constantly evaluate how good their current position is and the directional change is determined by a combination of their evaluation and the collective evaluation of the swarm.

For each iteration of the algorithm the agents are moved to a new position where a new evaluation is calculated. Depending on how good this evaluation is, and if there exist better results from the collective population, the position is either remembered or not, and the agents keep moving. This process is repeated until the algorithm terminates.

Walls are assigned to the solution space in such a way that agents will only consider solutions from inside. These walls represent limitations set upon the solution by mechanical and practical considerations.

B. PSO Design Proposal

Table III depicts the proposed design from the PSO. The PSO evaluated 11 variables which requires quite a lot of computational power. A supercomputer was used for the calculations, but difficulties surrounding the manual control of multithreading for a COMSOL model delayed the process quite a bit and prevented multiple iterations of the full PSO. The parametric limits could perhaps have been better defined.

The results show a machine with a much higher gear-ratio and fewer poles than the manual design. It did achieve a higher torque performance, but by looking at the proposed variables it is clear that an even higher torque could have been achieved. The reason for this is that the air-gap length proposed is higher than the lower limit of 3 mm, for both air-gaps. A thinner air-gap will return a higher torque, and therefore better solutions do exist. However, the PSO is a great tool for pointing out interesting solutions, when considering a new machine design, which in turn can be evaluated by the machine designer. As the design process evolves the limits of the PSO can be narrowed down following mechanical and power-system requirements and considerations, while still providing useful input to the final design.

VIII. LOSSES

The losses in AC machines are generally divided into four categories. These are copper losses, core losses, mechanical losses and stray losses [29]. Mechanical losses such as shaft friction and windage are not considered in this thesis. Neither are stray losses, which represents all losses that do not fit into

the other categories, such as end effects and flux leakage. The other effects are described in this section, and analyzed further in section IX.

A. Copper Losses

Copper losses are caused by the resistance of the current carrying copper wires in the armature windings. They depend on wire resistance and current in the machine following the relation $P_{loss} = 3R_a I_a^2$.

In this thesis the copper losses are calculated analytically after a method presented in [26]. DC resistance of a coil can be calculated as

$$R = \frac{L_{coil}}{\rho_{cu} A_{coil}}, \tag{20}$$

where L_{coil} is winding length in the direction of current flow, including end windings. ρ_{cu} is copper conductivity and A_{coil} is the area of the coil cross section. Adopting an approach from [36] the AC resistance is calculated as 1.2 times the DC resistance. Because the machine is current excited this is enough information to calculate the losses in each coil. The total number of coils is then $(P_i \cdot 3)$.

B. Core losses

Core losses are the combination of hysteresis losses, eddy-current losses and anomalous losses. Hysteresis loss is the energy required to align the domains of the ferromagnetic material in the direction of the magnetic field of the machine. Eddy current losses are resistive losses caused by circulating currents induced in the iron due to a time varying magnetic field. Anomalous losses are described in [37] as caused by intricate phenomena such as microstructural interactions, magnetic directional dependency and nonhomogenous locally induced eddy currents.

Calculation of core losses have traditionally been based on the assumption of sinusoidal flux density of varying magnitude and frequency [38], according to the Steinmetz equation [39]. However for higher flux densities than 1.0 T and for non linear magnetic materials this way of calculating losses is inaccurate. According to [38] a plurality of models have been proposed that try to correct and modify the initial models, but these models do not account for anomalous losses or consider flux harmonics. [38] also points out that measured values are systematically higher than the classical estimated values, which have been countered by adding corrective parameters in magnitudes surpassing two. The classical "evolved" method of estimating losses under sinusoidal conditions is referred to as

$$\begin{aligned} P &= P_h + P_e + P_a & (21)\\ &= k_h f B^{\alpha} + k_e f^2 B^2 + k_a f^{1.5} B^{1.5}, & (22) \end{aligned}$$

where P_h is hysteresis losses, P_e is eddy current losses and P_a denotes anomalous losses. For the classical model K_h, K_e and K_a are constant material coefficients for hysteresis-, eddy-current- and anomalous losses, while f is the frequency of the magnetic field and B is the flux density. However it has been shown that the coefficients K_h, K_e and K_a are less constant in practice than the classical model. [37] and [38] are among papers devoted to showing this non-linearity.

The underestimation of losses in the classical model is blamed by [38] on the waveform distortion, the complexity of machine structures and complex behavior of dynamic hysteresis loops. To improve this it is proposed to evaluate the magnetic fields at any point in the structure and develop a dynamic model that accounts for varying frequencies and flux densities.

In the case of the GE-MGEM studied in this thesis, the operation depends on the existence of flux harmonics and it is therefore believed that the traditional methods are inaccurate for calculating core losses. A method based on evaluating the field in each element of the mesh is therefore adopted. The method finds the frequency and flux density of each domain before calculating the core losses. This method is used for the yoke of both the stator and the rotor.

Losses in the PMs and in the iron pole-pieces of the rotor are estimated Comsol by making each PM and each pole-pair a single turn coil. From this approximate losses can be calculated.

Steel manufacturers do normally not provide the loss coefficients directly. Instead they provide data for losses per kilogram for a frequency of 50 or 60 Hz [40], [41], which is the nominal frequency of most power systems. It is beyond the scope of this thesis to gather the require material information necessary for estimating the material coefficients by mathematical regression. Instead the calculated yoke losses will be based on constants from [42].

C. Calculation of core losses in the GE-MGEM

Losses in the yoke of the machine is calculated with a matlab script that extracts the maximum flux density in each domain of the iron, and uses (22) on it. The values of the constants K_h, K_e and K_a are constant for simplicity.

IX. Analysis

A. Torque in the time domain

Both topologies were simulated in the time domain. The simulation struggled to converge when including magnetic saturation in the iron, however running the simulations without accounting for saturation results in a somewhat higher torque. In this analysis the time-simulations are performed without saturation, but the results are scaled with a factor that represents the relative difference between the calculated torque for the stationary solution of both models, with and without accounting for saturation. This can be expressed as

$$K_{\tau,c} = \frac{\tau_{max,saturated}|_{t=0}}{\tau_{max,unsaturated}|_{t=0}}, \tag{23}$$

where τ is torque and the subscript represents the condition. Torque values are per meter of the machine. The torque correction factor is not exact as it assumes a linear relationship between the results limited by saturation and those that are not. When accounting for magnetic saturation the history of the magnetic field affects the magnetization, in accordance

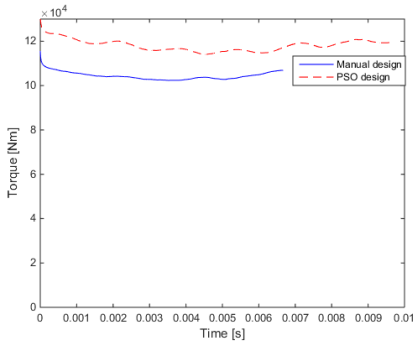

Fig. 20. Torque vs time for both designs

with the hysteresis loop [29]. In the time domain this means that the magnetization does not follow the external magnetic field instantaneously and these delays may cause variations in output torque. Because of these mechanisms the factor is only used to make the torque magnitudes more realistic. The effects on torque related to hysteresis is therefore not shown in this thesis.

The manually designed case has a scaling factor of $1.1588e5/1.2704e5 = 0.91$ while the PSO design has a factor of $1.2589e5/1.4375e5 = 0.88$. Applying these factors to the time-plots of torque results in the graph of Fig. 20, where torque is shown for one electrical period for both designs.

The different x-axis lengths of the two plots is because of the difference in synchronous frequency for the two designs. A dip in the torque can be observed at the beginning of each simulation, before the curve levels out. This is caused by the eddy currents in the ferromagnetic pole-pieces and the PMs. These currents are induced because the pole-pieces want to contradict the changing field, by setting up its own field according to Lenz/Faradays law. Initially these currents are zero, because the time derivate of the field is zero. Once the time-dependent solver has some data however, the eddy-currents start to appear.

Torque ripples are caused by a combination of cogging torque and flux-variations due to eddy currents. This ripple amounts to $\leq 4\%$ and $\leq 5\%$ of average torque for the manual and PSO design respectively.

Required axial length of the machines is calculated based on average output torque and the required output torque of 200 kNm. This results in axial lengths of 1.79 m and 1.67 m for the manual and the PSO design respectively.

B. Voltages and power-factors

The coil node of COMSOL 5.2a calculates the current and voltage waveforms in the machine windings. These are depicted for both the topologies in Fig. 21. With the machines being current excited, the angle of the current is known. A power factor can therefore be found by studying the phase shift of the current and voltage in the same phase. This shift

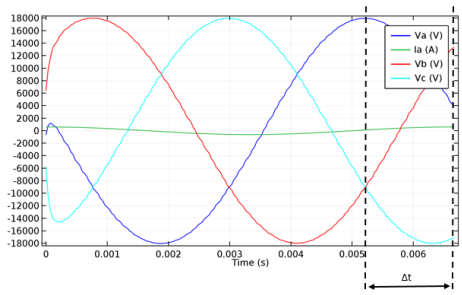

(a) Manual design

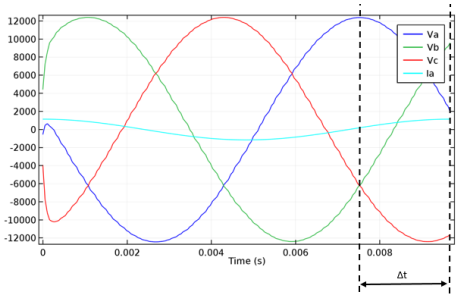

(b) PSO design

Fig. 21. Coil voltage waveforms for each design along with the current waveform of phase A

is denoted Δt in the figure. From this the power factor (PF) can be calculated as

$$\begin{aligned} \phi &= 2\pi f \Delta t \\ PF &= cos\phi, \end{aligned} \tag{24}$$

where ϕ is the phase shift and f is electrical frequency. The PF for the manual and the PSO design at maximum obtainable load is 0.187 and 0.188 respectively. While obtaining the PF it is common to compensate for total harmonic distortion (THD). However, this is not done in this thesis based on a qualitative consideration of the voltage waveform. These PF values are very poor compared to the claimed PF of ~ 0.9 in [6], while achieving a torque density of 110 kNm/m^3 for the large PDD mentioned in the introduction. Similarly [4] claimed that the PF can surpass 0.9. These numbers are for the PDD topology, but due to similar principles of operation, a certain correlation with the results from the GE-MGEM was expected. Low PFs are unfortunate because converter VA-ratings an PFs are inversely proportional, thus adding both cost and volume to the final solution.

However, there are some key differences in the modeling basis in these papers compared to this thesis along with many unknowns. Firstly the large machine in [6] has a diameter of 3.5 m which is 2.3 m larger than the designs in this thesis. This is believed to affect the torque density due to the scaling of the effective air-gap area following the approximate relation $\tau = kD^2l$ [43], which may outweigh the increase in volume $V = (D/2)^2\pi l$. D denotes outer diameter and l machine length. Secondly the air-gap lengths used in these papers are unknown and they may very well be lower than the 5 mm gaps used in this thesis. As shown in section VI-F the torque output depends

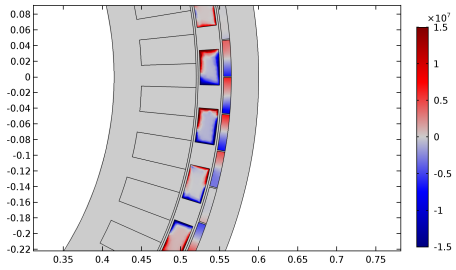

Fig. 22. Induced eddy currents in the pole-pieces and PMs

heavily on air-gap length, and by using a thinner air-gap the torque angle can be reduced while maintaining a high torque density, which may improve the power factor.

A more throughout analysis of the possibility to increase the power-factor should be conducted before scrapping the designs. Interestingly it seems that the machines suffer from the same challenges as the Vernier reluctance machines with low power factors. The low power-factor of hybrid vernier machines was shown by [44] to be an inherent feature of variable reluctance machines, and the GE-MGEM has been shown to share many features of the vernier PM machine as mentioned in III. Advanced methods of improving Vernier PM machine PF was proposed in [45], and could also be adopted by the GE-MGEM.

C. Losses

The losses in the machines are expected to be dominated by eddy current losses in the PMs and the pole-pieces. This is because these parts consist of non-laminated material which allows currents to flow freely in axial direction. Fig. 22 shows a surface plot of the induced eddy currents in the pole-pieces and the PMs.

1) PM and pole-piece losses: An internal COMSOL function calculates the power dissipation density in the pole-pieces and PMs. This is also called Joule Heating and is expressed as $Q = \mathbf{JE}$, where $\mathbf{J}$ represents the current density vector and $\mathbf{E}$ represents the electric field vector. The results for the pole-pieces and PMs respectively are 440 and 535 kW/m for the manual design and 700 and 385 kW/m for the PSO design. These losses are very high, and measures should be taken to reduce them. Such measures could be sectioning the PMs or laminating the steel pole-pieces. Regarding the pole-pieces, they were assumed not to be laminated due to rotor strength requirements, and this causes very large eddy currents.

2) Yoke core losses: Yoke losses are hard to predict for machines with a large number of large flux harmonics. For the calculation of these losses a script that follows the method described in section VIII is used. The sript is developed by [46] and identifies the flux density and frequency of each mesh domain. It then uses (22) to evaluate the losses. For this case the constants used are for non grain oriented laminated steel 50pn270 at 150 Hz. The constants used are $K_e = 3.8724 \cdot 10^{-5}$, $K_h = 0.01838$ and $K_a = 0.0004$ aquired from [42].

The resulting yoke core losses are 46 and 42 kW/m for the manual and PSO design respectively. As expected these losses are lower than in the non laminated pole-pieces.

3) Resistive losses: Copper losses are calculated with the analytical formula for DC resistance in (20) multiplied with a factor of 1.2 to estimate AC resistance. Current follows from the number of turns and the external current density of the model. The length of each coil can be expressed as

$$L_{coil} = 2L_{axial} + 2L_{end}, \tag{25}$$

where L_{axial} is total axial lenth of the machine and L_{end} is the length of the end windings. The axial length of the machine is given in IX-A. End winding length depends on winding principle. For the models in this thesis this is defined as the circumferential length of one pole-pitch angle for a radius to the centre of the slots. By choosing the circumferential length instead of the shortest distance, the additional length required to interleave the end windings is accounted for.

Inserting the dimensions from the model in (25) and (20) results in a resistance of $3.25 \cdot 10^{-5}$ and $1.53 \cdot 10^{-5}$ for the manual and pso design windings and correspondingly copper losses are 145 W and 121 W.

X. Conclusion

A design process for a magnetic gear electric machine topology has been performed by the use of FEM simulations. The design process was meticulously performed in an iterative approach assisted by simulations. In addition to this a full particle swarm optimization algorithm was completed, subject to the same parameter constraints. It was shown to be a powerful tool for assisting a design process, and it proposed a design with better performance than the manual method achieved.

Both the proposed designs where analyzed by FEM simulations. The topologies achieved very high torque per machine volume, as high as 98.8 kNm/m^3 and 105.9 kNm/m^3 respectively, which is beneficial when space is limited. Time domain simulations however, resulted in power factors of 0.187 and 0.188 for the two designs respectively, which is very poor. This requires very large converters, which is a very clear disadvantage in marine applications. Losses were also calculated, and the PM and pole-piece core losses where found to dominate.

Throughout this thesis the relation between the magnetic gear machines and the Vernier PM machines has been investigated, and it can be concluded that they are very similar. Poor power-factors are an inherent problem in Vernier PM machines and it seems like the analyzed machines are subject to the same challenges.

Initial thoughts are therefore that the torque density advantage these designs have over state of the art PM machines is outweighed by the much poorer power factors, and it is perhaps time to consider different topologies.

Further work could include investigation of how to improve the power factor, without loosing the extraordinary torque

density. It may also include renaming the topology to a Vernier partitioned stator machine.

ACKNOWLEDGMENT

The author would like to thank Prof. Robert Nilssen for first class supervising, as well as Dr.Eng. Alexey Matveev, Eirik Mathias Husum and the other employees at Rolls Royce marine AS for excellent guidance.

A gratitude is also extended to fellow student Sol Maja Fossen for performing the PSO on a supercomputer. Fellow office members Stian Bjornes and Usman Hassan deserve an acknowledgment for their input, and a special thanks is directed to Lasse Kløvstad for helping out with loss calculations.

REFERENCES

[1] K. Atallah and D. Howe, "A novel high-performance magnetic gear," *IEEE Transactions on magnetics*, vol. 37, no. 4, pp. 2844–2846, 2001.

[2] E. Gouda, S. Mezani, L. Baghli, and A. Rezzoug, "Comparative study between mechanical and magnetic planetary gears," *IEEE Transactions on Magnetics*, vol. 47, no. 2, pp. 439–450, 2011.

[3] W. Michal-Wolfgang, J. Hemmelmann, R. Qu, and P. L. Jansen, "Electric machine apparatus with integrated, high torque density magnetic gearing," US Patent US8 358 044, 2006.

[4] K. Atallah, J. Rens, S. Mezani, and D. Howe, "A novel "pseudo" direct-drive brushless permanent magnet machine," *IEEE Transactions on Magnetics*, vol. 44, no. 11, pp. 4349–4352, 2008.

[5] K. Chau, D. Zhang, J. Jiang, C. Liu, and Y. Zhang, "Design of a magnetic-geared outer-rotor permanent-magnet brushless motor for electric vehicles," *IEEE Transactions on Magnetics*, vol. 43, no. 6, pp. 2504–2506, 2007.

[6] D. Powell, S. Calverley, F. De Wildt, and K. Daffey, "Design and analysis of a pseudo direct-drive propulsion motor," in *Power Electronics, Machines and Drives (PEMD 2010), 5th IET International Conference on*. IET, 2010, pp. 1–2.

[7] C. Bjørk, "A comparison of integrated magnetic gear electric machines for marine propulsion," *Specialisation project, NTNU*, 2016.

[8] K. Elgmork, *Vitenskapelig metode*. Universitetsforlaget, 1985.

[9] M. J. T. B., "Magnetic transmission," US Patent US3 378 710, 1964.

[10] D. Hesmondhalgh and D. Tipping, "A multielement magnetic gear," in *IEE Proceedings B-Electric Power Applications*, vol. 127, no. 3. IET, 1980, pp. 129–138.

[11] K. Tsurumoto and S. Kikuchi, "A new magnetic gear using permanent magnet," *IEEE Transactions on Magnetics*, vol. 23, no. 5, pp. 3622–3624, 1987.

[12] K. J. Strnat, "Modern permanent magnets for applications in electrotechnology," *Proceedings of the IEEE*, vol. 78, pp. 923 – 946, 1990.

[13] P. O. Rasmussen, T. O. Andersen, F. T. Jorgensen, and O. Nielsen, "Development of a high-performance magnetic gear," *IEEE Transactions on Industry Applications*, vol. 41, no. 3, pp. 764–770, 2005.

[14] K. Atallah, S. Calverley, and D. Howe, "Design, analysis and realisation of a high-performance magnetic gear," *IEE Proceedings-Electric Power Applications*, vol. 151, no. 2, pp. 135–143, 2004.

[15] E. Gouda, S. Mezani, L. Baghli, and A. Rezzoug, "Comparative study between mechanical and magnetic planetary gears," *IEEE Transactions on Magnetics*, vol. 47, no. 2, pp. 439–450, 2011.

[16] L. Wang, J. Shen, Y. Wang, and K. Wang, "A novel magnetic-geared outer-rotor permanent-magnet brushless motor," *4th IET International Conference on Power Electronics, Machines and Drives*, pp. 33 – 36, 2008.

[17] L. Wang, J.-X. Shen, P. C.-K. Luk, W.-Z. Fei, C. Wang, and H. Hao, "Development of a magnetic-geared permanent-magnet brushless motor," *IEEE Transactions on magnetics*, vol. 45, no. 10, pp. 4578–4581, 2009.

[18] Z. Zhu and D. Evans, "Overview of recent advances in innovative electrical machines—with particular reference to magnetically geared switched flux machines," in *Electrical Machines and Systems (ICEMS), 2014 17th International Conference on*. IEEE, 2014, pp. 1–10.

[19] A. Toba and T. A. Lipo, "Generic torque-maximizing design methodology of surface permanent-magnet vernier machine," *IEEE transactions on industry applications*, vol. 36, no. 6, pp. 1539–1546, 2000.

[20] K. Mukherji and A. Tustin, "Vernier reluctance motor," in *Proceedings of the Institution of Electrical Engineers*, vol. 121, no. 9. IET, 1974, pp. 965–974.

[21] D. Rhodes, "Assessment of vernier motor design using generalised machine concepts," *IEEE Transactions on Power Apparatus and Systems*, vol. 96, no. 4, pp. 1346–1352, 1977.

[22] S. Gerber and R.-J. Wang, "Design and evaluation of a pm vernier machine," in *Energy Conversion Congress and Exposition (ECCE), 2015 IEEE*. IEEE, 2015, pp. 5188–5194.

[23] J. N. Fjellanger, "Gearing as a part of an electric machine functionally," Master's thesis, NTNU, 2016.

[24] R. Qu, D. Li, and J. Wang, "Relationship between magnetic gears and vernier machines," in *Electrical Machines and Systems (ICEMS), 2011 International Conference on*. IEEE, 2011, pp. 1–6.

[25] C. Lee, "Vernier motor and its design," *IEEE Transactions on Power Apparatus and Systems*, vol. 82, no. 66, pp. 343–349, 1963.

[26] D. Hanselman, *Brushless Permanent Magnet Motor Design*, 2nd ed. Magna Physics Publishing, 2003.

[27] A. Arkkio *et al.*, *Analysis of induction motors based on the numerical solution of the magnetic field and circuit equations*. Helsinki University of Technology, 1987.

[28] J. Coulomb, "A methodology for the determination of global electromechanical quantities from a finite element analysis and its application to the evaluation of magnetic forces, torques and stiffness," *IEEE Transactions on Magnetics*, vol. 19, no. 6, pp. 2514–2519, 1983.

[29] S. Chapman, *Electric machinery fundamentals*, 5th ed. McGraw-Hill, 2012.

[30] Information about vilje. [Online]. Available: https://www.hpc.ntnu.no/display/hpc/Vilje

[31] Z. Zhu and D. Howe, "Influence of design parameters on cogging torque in permanent magnet machines," *IEEE Transactions on energy conversion*, vol. 15, no. 4, pp. 407–412, 2000.

[32] S. M. B. Fossen, "Untitled thesis on enabling technologies," Master's thesis, NTNU, 2017.

[33] K. I. Bergset, "Developing a numerical model for optimization of a coaxial magnetic gear," Master's thesis, NTNU, 2016.

[34] E. L. Engevik, A. Røkke, and R. Nilssen, "Evaluating hybrid optimization algorithms for design of a permanent magnet generator," in *Electrical Machines & Power Electronics (ACEMP), 2015 Intl Conference on Optimization of Electrical & Electronic Equipment (OPTIM) & 2015 Intl Symposium on Advanced Electromechanical Motion Systems (ELECTROMOTION), 2015 Intl Aegean Conference on*. IEEE, 2015, pp. 711–718.

[35] R. Eberhart and J. Kennedy, "A new optimizer using particle swarm theory," in *Micro Machine and Human Science, 1995. MHS'95., Proceedings of the Sixth International Symposium on*. IEEE, 1995, pp. 39–43.

[36] A. Rokke, "Gradient based optimization of permanent magnet generator design for a tidal turbine," in *Proceedings of the 2014 International Conference on Electrical Machines (ICEM), Berlin, Germany*, 2014, pp. 2–5.

[37] D. M. Ionel, M. Popescu, S. J. Dellinger, T. Miller, R. J. Heideman, and M. I. McGilp, "On the variation with flux and frequency of the core loss coefficients in electrical machines," *IEEE Transactions on Industry Applications*, vol. 42, no. 3, pp. 658–667, 2006.

[38] Y. Chen and P. Pillay, "An improved formula for lamination core loss calculations in machines operating with high frequency and high flux density excitation," in *Industry Applications Conference, 2002. 37th IAS Annual Meeting. Conference Record of the*, vol. 2. IEEE, 2002, pp. 759–766.

[39] C. P. Steinmetz, "On the law of hysteresis," *Transactions of the American Institute of Electrical Engineers*, vol. 9, no. 1, pp. 1–64, 1892.

[40] Jfe steel, electrical steels product catalog. [Online]. Available: http://www.jfe-steel.co.jp/en/products/electrical/catalog/f1e-001.pdf

[41] Aks steel, electrical steels product catalog. [Online]. Available: http://www.aksteel.com/pdf/markets_products/electrical/mag_cores_data_bulletin.pdf

[42] Emetor material database. [Online]. Available: https://www.emetor.com/edit/materials/sura-m270-35a/?cat=6&co=10

[43] J. Bone, "Influence of rotor diameter and length on the rating of induction motors," *IEE Journal On Electric Power Applications*, vol. 1, no. 1, pp. 2–6, 1978.

[44] E. Spooner and L. Haydock, "Vernier hybrid machines," *IEE Proceedings-Electric Power Applications*, vol. 150, no. 6, pp. 655–662, 2003.
[45] D. Li, R. Qu, and T. A. Lipo, "High-power-factor vernier permanent-magnet machines," *IEEE Transactions on Industry Applications*, vol. 50, no. 6, pp. 3664–3674, 2014.
[46] L. Kløvstad, "Comparing the surface- and interior permanent magnet machine with concentrated windings for high dynamic applications," Master's thesis, NTNU, 2017.

APPENDIX A
ADDITIONAL SIMULATION RESULTS

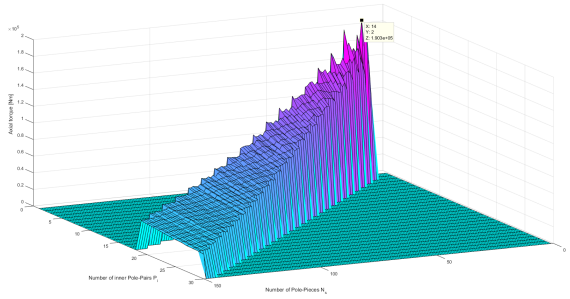

Fig. 23. Torque vs number of pole-pieces N_s and armature pole-pairs P_i without accounting for the effects of magnetic saturation

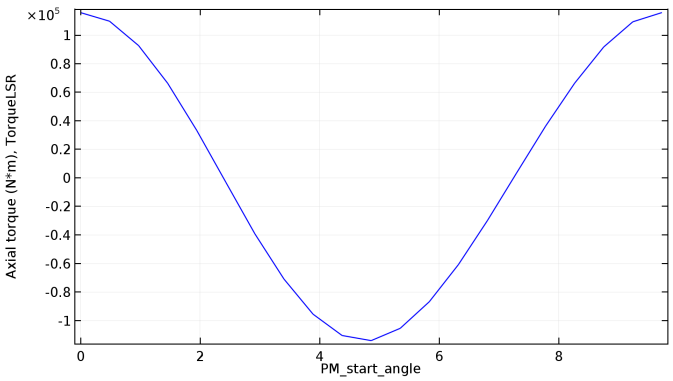

Fig. 24. Torque as a function of PM rotation

APPENDIX B
SPECIFIC MODEL INFORMATION

A. Copper Loss Calculation

Variable	Manual value	PSO value
r_{slot}	0.485 m	0.4257 m
pole-pitch	0.3926 rad	0.7854 rad
L_{end}	0.19 m	0.43 m
L_{axial}	1.79 m	1.67 m
L_{coil}	3.96 m	4.2 m
A_{coil}	0.00244 m^2	0.00459 m^2
I_{rms}	432 A	812 A

TABLE IV
DATA

$\rho_{cu} = 6e7 S/m$

B. B-H curve

Silicon Steel curve:

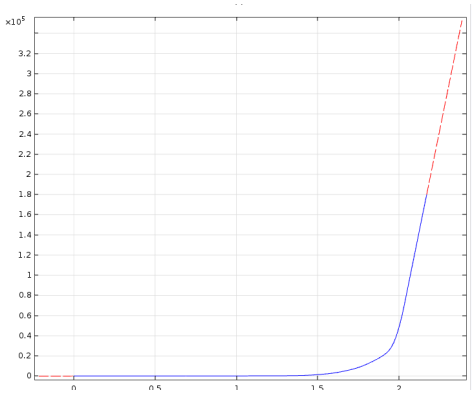

Fig. 25. Saturation curve of Silicon Steel 50PN270

$$
\begin{aligned}
R_{AC} = 1.2R_{DC} &= 1.2\frac{L_{coil}}{\rho_{cu} A_{coil}} \\
R_{Manual} &= 1.2\frac{3.96}{6e7 \cdot 0.00244} = 3.25 \cdot 10^{-5}\Omega \\
R_{PSO} &= 1.2\frac{4.2}{6e7 \cdot 0.00459} = 1.525 \cdot 10^{-5}\Omega \\
P_{loss,manual} &= 8 \cdot 3 \cdot 432^2 \cdot 3.25 \cdot 10^{-5} = 145.6W \\
P_{loss,PSO} &= 4 \cdot 3 \cdot 812^2 \cdot 3.25 \cdot 10^{-5} = 120.7W
\end{aligned}
\tag{26}
$$

APPENDIX C
MATLAB SCRIPTS

A. Matlab Pole-Pair list generator

```
1
2  clc
3  clear all
4
5  %P_i range 2:1:30
6  %N_s range 10:1:150
7
8  fileID=fopen('ParamList.txt','w');
9  i=0;
10
11 fprintf(fileID, 'P_i ');
12
13 for p=2:1:30
14     for n=10:1:150
15         if (n>p && ((n/p)≤8) && ((n/p)≥5))
16             fprintf(fileID, '%d ',p);
17             i=i+1;
18         end
19     end
20 end
21
22 fprintf(fileID, '\r\nN_s ');
23
24 for p=2:1:30
25     for n=10:1:150
26         if (n>p && ((n/p)≤8) && ((n/p)≥5))
27
28             fprintf(fileID, '%d ',n);
29         end
30     end
```

```
31  end
32
33  fclose(fileID);
```